3D RECONSTRUCTION OF SMALL SOLAR SYSTEM BODIES USING PHOTOCLINOMETRY BY DEFORMATION

CAPANNA Claire [1,2], JORDA Laurent [1], LAMY Philippe [1]
(1) Laboratoire d'Astrophysique de Marseille
38 rue Joliot Curie, 13388 Marseille Cedex 13, France

GESQUIERE Gilles [2]
(2) Laboratoire des Sciences de l'Information et des Système
rue R. Follereau, BP 90178, 13637 Arles Cedex

ABSTRACT

This article considers the problem of reconstructing the 3D shape model of asteroids and cometary nuclei from images obtained with an imaging system on board a spacecraft. We present a photoclinometry method based on the minimization of the chi-square difference between observed and synthetic images of the object by deformations of its initial shape. The minimization is performed using the so-called "limited-memory Broyden-Fletcher-Golbfarb-Shanno" algorithm. The deformations can be applied: (i) by modifying the coefficients of a spherical harmonic expansion in order to extract the global shape of the object, and/or (ii) by moving the height of the vertices of a triangular mesh in order to increase the accuracy of the global shape model and/or to derive localized topographic maps of the surface. This method has been tested on images of the asteroids Steins and Lutetia observed by the imaging system on board the Rosetta spacecraft of the European Space Agency.

KEYWORDS

3D reconstruction, optimization, deformation, synthetic images, photoclinometry

1. INTRODUCTION

There are several ways to reconstruct a three-dimensional surface from the grey levels measured in the pixels of an image. The stereo technique allows to build a network of control points from remarkable features identified at the surface of the object [8]. Stereo-photogrammetry, an extension of the former, is a powerful technique widely used in the past to reconstruct digital terrain models, for instance that of planets [3] or that of the nuclei of comets [6]. More recently, stereophotoclinometry using several views of the same area of the surface under different viewing and/or illumination conditions has been successfully applied to several bodies of our solar system, among them the asteroid Itokawa observed by the Hayabusa spacecraft [2].

We present here a new photoclinometry method in which we apply deformations to a triangular mesh in a non-linear optimization loop until the synthetic images resulting from the mesh best match the observed ones. The article is organized as follows: we present our method in Section 2, its application to asteroids Steins and Lutetia in section 3 and we finally conclude in Section 4.

2. 3D RECONSTRUCTION METHOD

Our 3D reconstruction method needs an input model described as a mesh of triangular facets. This model can be a sphere or a more refined model obtained with another reconstruction method.

2.1 Generation of synthetic images

Synthetic images are generated using a tool called OASIS (Optimized Astrophysical Simulator for Imaging Systems) [5]. OASIS calculates the position and the orientation of the object in the camera frame. It then performs ray-casting to determine which facets of the shape model are illuminated and in view of the camera. For each such facet i and each image n, it calculates the bi-directional reflectance (BDR) $r_i^{(n)}$ following Hapke's model [4]. The intersections $\Omega_i^{(p,q,n)}$ between this facet and the pixel (p, q) are calculated in terms of solid angle. The signal $D_{pq}^{(n)}$ received by each pixel (in DN) is then estimated by summing the contributions of all facets in the field-of-view of this pixel:

$$D_{pq}^{(n)} \approx \frac{g\, S_{coll}\, t_e^{(n)}}{hc\, (R_h^{(n)})^2} \left(\sum_{i=1}^{M_{pq}} r_i^{(n)}\, \Omega_i^{(p,q,n)}\, \rho_i \right) \qquad (1)$$

where g is the gain of the electronics, S_{coll} is the collecting surface of the telescope, $t_e^{(n)}$ is the exposure time of image n, $R_h^{(n)}$ is the heliocentric distance of the object (in astronomical units), h is Planck's constant, c is the light speed, ρ_i is a pre-calculated absolute calibration factor. Finally, the image is convolved by the point-spread-function of the instrument.

2.2 Deformations of the shape model

2.2.1 Deformation based on Spherical Harmonics

Spherical parametrization of a triangular mesh shape model has been developed in the last three decades. The spherical harmonic transform [10] is used to decompose the input model in the frequency domain. The coordinates $\mathbf{R'_k}$ of the vertices are described as:

$$\mathbf{R'_k} = R_k \begin{pmatrix} \sin\theta_k\, \cos\varphi_k \\ \sin\theta_k\, \sin\varphi_k \\ \cos\theta_k \end{pmatrix} \qquad (2)$$

where (θ_k, φ_k) defines the vertices of a pre-defined triangular mesh in a spherical coordinates system and R_k is given by:

$$R_k = \sum_{l=0}^{l_{max}} \sum_{m=-l}^{+l} C_{lm} Y_{lm}(\theta_k, \varphi_k) \qquad (3)$$

$Y_{lm}(\theta, \varphi)$ are the real form of the spherical harmonic functions. In this representation, the parameters C_{lm} define the shape of the object. The number of coefficients depends on the degree l_{max} of the above expansion. Increasing its value allows us to get higher frequencies in the 3D representation of the object.

2.2.2 Deformation based on vertex offsets

In order to increase the accuracy of the spherical harmonic model or of the input model, we introduce another deformation scheme in which we directly modify the height of the vertices with respect to the initial mesh used as starting points in the optimization process. We calculate the vector $\mathbf{N_k}$ normal to the surface at the vertex k by averaging the normal vectors $\mathbf{N_i}$ of the V_k facets which share this vertex:

$$\mathrm{N_k} = \frac{\sum_{i=1}^{V_k} S_i\, \mathrm{N_i}}{\sum_{i=1}^{V_k} S_i} \qquad (4)$$

where S_i is the surface of the facet number i .

The modification of the height H_k of the vertex k is applied in the direction $\mathbf{N_k}$. The coordinates $\mathbf{R'_k}$ of the vertex after this deformation become:

$$\mathrm{R'_k} = \mathrm{R_k} + H_k\, \mathrm{N_k} \qquad (5)$$

The coefficients H_k are initially set to zero and their value is modified during the optimization.

2.3 Optimization of the parameters

2.3.1 Shape model

We want to minimize the reduced chi-square between the pixel values $F_{pq}^{(n)}$ of the N observed images and those of the synthetic images given by Eq. (1):

$$\chi^2(P_k) = \frac{1}{N_p} \sum_{n=1}^{N} \sum_{pq} \frac{\left(F_{pq}^{(n)} - D_{pq}^{(n)}(P_k)\right)^2}{(\sigma_{pq}^{(n)})^2} \qquad (6)$$

where N_p is the total number of pixels used in the minimization process, and $\sigma_{pq}^{(n)}$, the uncertainty on the observed pixel value, is given by:

$$\sigma_{pq}^{(n)} = g \sqrt{\frac{D_{pq}^{(n)}\, t_e}{g} + \sigma_R^2} \qquad (7)$$

where σ_R is the readout noise. In Eq. (6), the free parameters (variables) P_k are the coefficients C_{lm} when the shape model is defined as an expansion in spherical harmonics (section 2.2.1) and the heights H_k when we modify the coordinates of the vertices (section 2.2.2).

In order to minimize the chi-square function (6), we use a non-linear optimization algorithm called "limited memory Broyden-Fletcher-Golbfarb-Shanno" (L-BFGS), a quasi-Newton optimization method [1]. It is well suited to large scale optimization problems and requires a limited amount of memory. A typical number of ~ 50 - 100 iterations of the algorithm is required before it converges to a stable value P_k of the free parameters. When the final parameters are reached, the coordinates $\mathbf{R'_k}$ of the vertices form the final shape model.

The L-BFGS method requires the calculation of the partial derivatives at each iteration. These derivatives are calculated with the finite difference method, in which two chi-squares are calculated with the Eq. (6) for each partial derivative:

$$\frac{\partial \chi^2}{\partial H_l}(H_k) = \frac{\chi^2(H_{k'}, H_l + \epsilon_H) - \chi^2(H_{k'}, H_l - \epsilon_H)}{2.\epsilon_H} \qquad (8)$$

where the index $k' = 1, ..., l\text{-}1, l\text{+}1, ..., N_v$, where N_v is the number of vertices.

We emphasize that a major part of the CPU time is used for the calculation of these derivatives. We will see in section 2.4 how these partial derivatives can be calculated much faster, thus allowing us to speed up considerably the optimization process.

2.3.2 Local error calculation

For each pixel *(p, q)* of the image number *n*, we calculate the residual value in units of the instrumental noise at the end of the optimization using the notation of section 2.3.1:

$$\mu_{pq}^{(n)} = \frac{F_{pq}^{(n)} - D_{pq}^{(n)}(P_k)}{\sigma_{pq}^{(n)}} \qquad (9)$$

We "project" the value of the residuals from the pixels to the facets using the pixel–facets intersecting solid angles $\Omega_i^{(p,q,n)}$ calculated earlier in section 2.1:

$$\mu_i = \frac{1}{N\,\Omega_P} \sum_{n=1}^{N} \sum_{pq} \Omega_i^{(p,q,n)}\, \mu_{pq}^{(n)} \qquad (10)$$

where Ω_P is the total pixel solid angle, and the second sum runs over the pixels *(p, q)* intersecting the facet number *i*. We then calculate the effect of a variation of the slope of each facet on the measured signal, normalized to its associated instrumental noise. The derivative $dD_i/d\varepsilon$ (in DN/°) of the signal with respect to a change of slope is obtained numerically by calculating the mean variation of the signal $D_i^{(n)}$ from Eq. (1) when the vector normal to each facet remains on a cone of axis $\mathbf{N_i}$ - the normal to the surface of the facet – and of half cone aperture ε. The error ξ_i on the slope of each facet is deduced from μ_i , $dD_i/d\varepsilon$, and from the instrumental noise σ_i associated to the signal D_i (Eq. 7):

$$\xi_i = \frac{|\mu_i| \sigma_i}{dD_i/d\epsilon} \qquad (11)$$

We take a typical value of $\varepsilon \sim 1°$ to estimate the value of the derivative $dDi/d\varepsilon$. Knowing the error on the slope, the error on the heights (parameters H_k) can be easily deduced. The parameter ξ_i forms what we call the "slope error map".

2.3.3 Additional parameters

Additional parameters can be optimized in the same way if they have an impact on the synthetic images, for instance:

– the parameters which describe the BDR of the surface,

– the three angles describing the pointing direction and roll angle of the camera for each individual image,

– the three Euler angles describing the orientation of the object in space.

The accuracy in the reconstruction of these parameters by the space agencies is usually not sufficient to successfully achieve the optimization process. Therefore, we always need to perform iterative optimizations of the shape, of the pointing direction and roll angle of the camera.

2.4 Faster calculation of the partial derivatives

2.4.1 General principle of the method

As explained in section 2.3.1, most of the CPU time during the optimization process is used to calculate the partial derivatives of Eq. (8). In this section, we describe a method that allows to calculate them faster, accelerating considerably the whole reconstruction process. The relationship (8) implies the calculation of two chi-squares, i.e. the calculation of 2*N* synthetic images for each partial derivative. We briefly describe in this section how we can perform the same task recalculating only the pixel values of the images which are modified when we move the height of a vertex from H_l to $H_l \pm \varepsilon_H$ (section 2.4.2) and to extract from these values the final partial derivative of the chi-square (section 2.4.3).

2.4.2 Calculation of updated pixel values

The calculation of the pixel values modified by a change of the height of the vertex number *l* from its original value H_l to $H_l \pm \varepsilon_H$ is performed in the following steps.

1) We identify the facets $\mathrm{F}_l^{(n)}$ using the vertex number *l*. We determine the nominal set of pixels $\mathrm{S}_l^{(n)}$ intersected by the facets. We then determine a new set of pixels $\mathrm{S}_{l,\pm}{}^{(n)}$ intersected by the facets after the height of the vertex number *l* has been modified. The set of pixels potentially modified by a displacement of this vertex is the union of both samples: $\mathrm{P}_l^{(n)} = \mathrm{S}_l{}^{(n)} \cup \mathrm{S}_{l,\pm}{}^{(n)}$.

2) We re-determine if the facets intersected by the pixels $\mathrm{P}_l^{(n)}$ are illuminated and visible from the observer taking into account the displacement of the vertex.

3) For all the facets $\mathrm{F}_l^{(n)}$ which are both illuminated and in view from the observer, we re-calculate the BDR $r_l^{(n)}$ taking into account the new geometry.

4) The updated values $D'_{pq}{}^{(n)}(H_k)$ of the pixels $\mathrm{P}_l^{(n)}$ are then calculated using the relationship (1).

We repeat this operation for all images (n = 1..*N*).

2.4.3 Chi-square partial derivatives calculation

Let us introduce the contribution of the image number *n* to the global chi-square of Eq. (6):

$$\gamma^{(n)} = \sum_{pq} \Delta_{pq}^{(n)} \qquad (12)$$

where:

$$\Delta_{pq}^{(n)} = \frac{\left(F_{pq}^{(n)} - D_{pq}^{(n)}(H_k)\right)^2}{(\sigma_{pq}^{(n)})^2} \quad (13)$$

The value of the function $\Delta'^{(n)}_{pq}$ corresponding to the updated pixel values $D'^{(n)}_{pq}(H_k)$ calculated in section 2.4.2 is calculated in the same way:

$$\Delta'^{(n)}_{pq} = \frac{\left(F_{pq}^{(n)} - D'^{(n)}_{pq}(H_k)\right)^2}{(\sigma_{pq}^{(n)})^2} \quad (14)$$

for $pq \in P_l$. We now call $A^{(n)}$ the set of all pixels of image number n. After modification of the height of a vertex, the pixels which remain unchanged belong to $C_l^{(n)}$. Using these notations, we have $A^{(n)} = C_l^{(n)} \cup P_l^{(n)}$. With these notations, the modified chi-square can be written as:

$$\chi'^2 = \frac{1}{N_p} \sum_{n=1}^{N} \left[\sum_{pq \in C_l^{(n)}} \Delta_{pq}^{(n)} + \sum_{pq \in P_l^{(n)}} \Delta'^{(n)}_{pq} \right] \quad (15)$$

which can be rewritten:

$$\chi'^2 = \frac{1}{N_p} \sum_{n=1}^{N} \left[\left(\gamma^{(n)} - \sum_{pq \in P_l^{(n)}} \Delta_{pq}^{(n)} \right) + \sum_{pq \in P_l^{(n)}} \Delta'^{(n)}_{pq} \right] \quad (16)$$

This relationship gives us the expression of the chi-square as a function of three parameters. The first parameter, $\gamma^{(n)}$, is calculated from the nominal image before the calculation of the partial derivatives. The parameters $\Delta_{pq}^{(n)}$ and $\Delta'^{(n)}_{pq}$ are recalculated knowing the sets of modified pixel $P_l^{(n)}$ of all images and the new pixel values $D'_{pq}(H_k)$.

The partial derivatives can be calculated with the finite difference of the new chi-square:

$$\frac{\partial \chi^2}{\partial H_l}(H_k) = \frac{\chi'^2(H_{k'}, H_l + \epsilon_H) - \chi'^2(H_{k'}, H_l - \epsilon_H)}{2.\epsilon_H} \quad (17)$$

This calculation is simplified since only the sums of contributions $\Delta_{pq}^{(n)}$ and $\Delta'^{(n)}_{pq}$ have to be calculated:

$$\frac{\partial \chi^2}{\partial H_l}(H_k) = \frac{1}{2.N_p.\epsilon_H} \sum_{n=1}^{N} \left[\sum_{pq \in P_{l,+}^{(n)}} \left(\Delta'^{(n)}_{pq}(H_{k'}, H_l + \epsilon_H) - \Delta_{pq}^{(n)}(H_{k'}, H_l + \epsilon_H) \right) - \sum_{pq \in P_{l,-}^{(n)}} \left(\Delta'^{(n)}_{pq}(H_{k'}, H_l - \epsilon_H) - \Delta_{pq}^{(n)}(H_{k'}, H_l - \epsilon_H) \right) \right] \quad (18)$$

The gain in CPU time in the calculation of the partial derivatives between the relationships (8) and (18) is then given by the ratio between the total number of pixels of the images and the typical number of pixels in all the set $P_l^{(n)}$, i.e., typically 4 pixels per image. The gain is therefore of the order of N_p / (4 N).

3. APPLICATIONS TO ASTEROIDS STEINS AND LUTETIA

3.1 Observations

The Rosetta spacecraft [7] launched in 2004 by the European Space Agency is now on its way to meet its final target, the nucleus of comet P/Churyumov-Gerasimenko. During its cruise, Rosetta flew by two asteroids: Steins in September 2008 and Lutetia in July 2010. Images of these two asteroids have been acquired by OSIRIS, the imaging system on board Rosetta. OSIRIS includes a narrow and a wide-angle

camera both equipped with the same 2048^2 pixels E2V 42-40 CCD detector offering pixel field-of-views of respectively 18.9 and 99.5 μrad.

Rosetta flew by Steins at a minimum distance of 802 km, with a phase angle which varied from 38° to 0° and then increased to almost 140° out-bound. For the following analysis, we use a set of 8 geometrically calibrated images: one image acquired with the narrow-angle camera from a distance of 5235 km and seven images acquired with the wide-angle camera from a distance of 1120 km in-bound (see Fig. 1) to 865 km out-bound. These images correspond to a range of phase angles from 7° to 73°.

Lutetia was flown by at a minimum distance of 3170 km, with a phase angle which varied from 10° to 0° and then increased to almost 140° out-bound. For the following preliminary tests, we use a set of 4 small images extracted from geometrically calibrated images acquired with the narrow-angle camera from a distance of 5200 km in-bound (see Fig. 3) to 3670 km out-bound. These images correspond to a range of phase angles from 26° to 110°.

3.2 Steins reconstruction

3.2.1 Reconstruction strategy

The shape reconstruction of Steins is performed in two main steps. The first step consists in calculating a low-resolution spherical harmonic model. For this, we start from a sphere, for which $C_{00} = R_a = 2.7\ km$ and the other parameters are set to zero. We use the Hapke parameters [4] describing the BDR derived from a global photometric analysis. We begin optimizing the C_{lm} spherical harmonic coefficients of the shape model with $l_{max} = 2$. We iteratively optimize the shape and the Euler angles describing the pointing of the camera. When a stable solution is reached, typically after 3-5 iterations, we set the degree of the expansion to $l_{max} = 4$ and we repeat the cycle of shape and Euler angles optimizations until $l_{max} = 20$. The sampling of the shape model is given by a hierarchical triangular mesh [9] of level five built from an icosahedron. The resulting 20480 facets and 10242 vertices ensure that the pixels of the images contain typically a few facets. At the end of this step, we have a spherical harmonic model of the asteroid. The corresponding synthetic image is given in Fig. 1.

In a second step, we optimize the heights of the vertices in order to improve the spherical harmonic shape model calculated at the previous step. We proceed as before by iteratively optimizing the shape model and the Euler angles. After a total of 3 iterations, the final shape model of the asteroid is obtained (see Fig. 1). We keep the same sampling of the surface used to derive the spherical harmonic shape model

The results given in this section were obtained with the “slow” version of chi-square partial derivative calculation, which corresponds to the Eq. (8).

3.2.2 Final shape model

Table 1 summarizes our results. The mean residuals are expressed in units of the instrumental noise. The final mean slope error is calculated from the residuals (section 2.3.2). Note that, for the spherical harmonic optimization, only one iteration between pointing and shape optimization is needed.

Table 1. Summary of our results for spherical harmonic Optimization (SHO) and Vertices Height Optimization (VHO)

Parameters	SHO	VHO
Starting chi-square	28640	90
Final chi-square	90	37
Mean residuals	9.5	6.1
Mean slope error	12°	7°
Mean height error	20 m	10 m
Number of iterations	1	3
Total CPU time	30 hours	3 weeks

The CPU times are given for a dual-core 2 GHz Opteron CPU with 2 GB of RAM. The mean residuals decrease from 9.5 to 6.1 (in units of instrumental noise) from the spherical harmonic to the triangular mesh representation (see also Fig. 1).

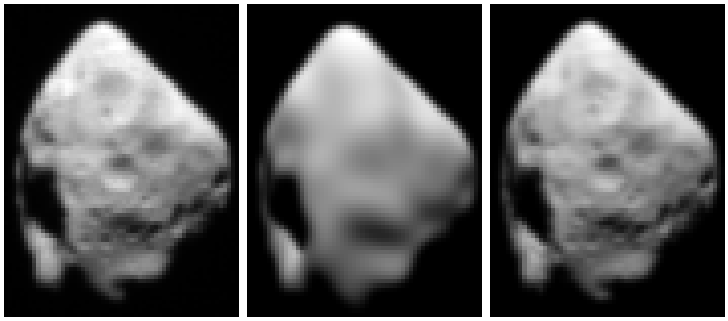

Figure 1. Illustration of the reconstruction methods for one of the eight images of asteroid Steins. Left panel: Observed image. Center panel: synthetic image calculated from spherical harmonic model. Right panel: synthetic image calculated from the final optimized model

3.2.3. Accuracy

We present in Fig. 2 the histogram of the values in the “slope error map” defined in section 2.3.2 for both the spherical harmonic model and the final triangular mesh model. For the latter, the histogram peaks at 7, which corresponds to 10 m in height, about 1/8th of the pixel resolution at closest approach.

Larger values of up to ~ 30° are however obtained in regions of the shape model which correspond to limbs or terminators on the images.

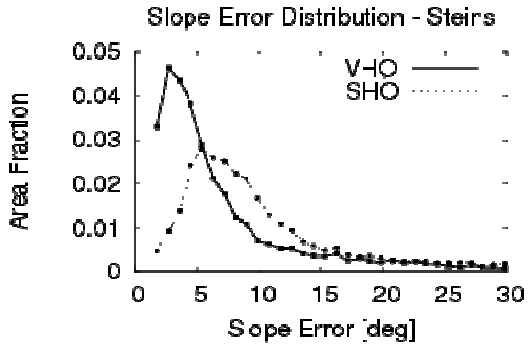

Figure 2. Slope Error Histogram of the models of Steins.

3.3 Preliminary Tests on Lutetia

Figure 3 shows the result of preliminary tests performed on a Digital Terrain Model of the asteroid Lutetia applying deformation on the height of the vertices. Our input model is a ``maplet'' (DTM) extracted from the Stereophotoclinometry model of R. Gaskell [2] calculated with his software LITHOS. Our method allows us to recover high-frequency information (right panel) compared to the initial DTM (middle panel). Craters and grooves are reconstructed with a more accurate depth.

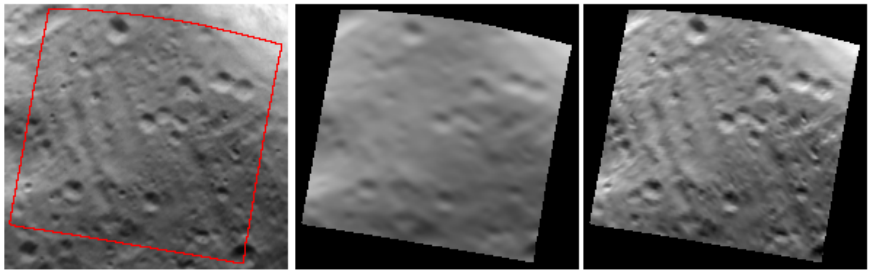

Figure 3. Illustration of the reconstruction method used on asteroid Lutetia. Left panel: Observed image. Center panel: synthetic image calculated from LITHOS model. Right panel: synthetic image calculated from the final optimized model

4. CONCLUSION AND FUTURE WORK

We developed and tested a new multi-image photoclinometry method based on deformations of a three-dimensional shape model, on images of the asteroid Steins obtained by the imaging system on board ESA's Rosetta spacecraft. The method also generates a map of the local topographic error deduced from the pixel residuals, both in slopes and in heights. In the case of Steins, the local averaged slope error amounts to 7°.

The "faster" version of the code for the calculation of the partial derivatives of the chi-square described in section 2.4 has been implemented in the code and is in the test and validation process. The first results indicate an overall gain in speed which is in agreement with the prediction, i.e., would correspond a factor of about 1000 for the example described in section 3, therefore reducing the total CPU time to 30 min.

In the near future, we intend to improve the speed and the robustness of the method by implementing it in a multi-resolution approach. We will also apply this technique to the Lutetia images in order to improve existing shape models of this asteroid. Finally, we will apply it to the images of the asteroid Vesta acquired by the DAWN spacecraft, and later on to the high-resolution images of the nucleus of comet 67P/Churuymov-Gerasimenko acquired by the scientific cameras of Rosetta.

REFERENCES

[1] Byrd, R.H. Et al., 1994, Representation of quasi-newton matrices and their use in limited memory methods, *Mathematical Programming* , Vol. 63, No. 4, pp. 129–156, 1994.

[2] Gaskell, R.W. et al., 2006, Landmark navigation studies and target characterization in the hayabusa encounter with itokawa, *AIAA, Astrodynamics Specialists Conference and Exhibit.*

[3] Gwinner, K. et al., 2007, Derivation and validation of high resolution digital terrain models from mars express HRSC-Data, *Photogramm. Eng. Remote Sens.*

[4] Hapke, B., 2002, Bidirectional reflectance spectroscopy 5. the coherent backscatter opposition effect and anisotropic scattering, *Icarus* , vol. 157, pp. 523-534.

[5] Jorda, L. et al., 2010, OASIS: a simulator to prepare and interpret remote imaging of solar system bodies, *Proc. SPIE*, Vol. 7533, No. 753311.

[6] Oberst, J. et al., 2004, The nucleus of Comet Borrelly: a study of morphology and surface brightness, *Icarus*, Vol. 167, pp. 70-79.

[7] Schulz, R., 2009, Rosetta - one comet rendezvous and two asteroid fly-bys, *Solar System Research* , Vol. 43, No. 4, pp. 343-352.

[8] Simonelli, D.P. Et al., 1993., The generation and use of numerical shape models for irregular solar system objects, Icarus , Vol. 103, pp. 49-61.

[9] Szalay, A. et al., 2005, Indexing the sphere with the hierarchical triangular mesh, *Tech. Rep. MSR-TR-2005-123, Microsoft Research*

[10] Wiebicke, H.J., 1989, A method for modelling the surface of irregular celestial bodies, *Astron. Nachr.* , Vol. 310, No.2, pp. 159–174.